Merging TEMPEST Microwave and GOES-16 Geostationary IR soundings for improved water vapor profiles

Chia-Pang Kuo[1], Christian Kummerow[1]

[1]Department of Atmospheric Science, Colorado State University, Fort Collins, CO 80523, USA

Correspondence to: Chia-Pang Kuo (chia-pang.kuo@colostate.edu)

Abstract. The Temporal Experiment for Storms and Tropical Systems Demonstration (TEMPEST-D) demonstrated the capability of CubeSat satellites to provide high-quality, stable microwave signals for estimating water vapor, clouds, and precipitation from space. Unlike the operational NOAA and MetOp series satellites, which combine microwave and hyperspectral infrared sensors on the same platforms to optimize retrievals, CubeSat radiometers such as TEMPEST do not carry additional sensors. In such cases, the high temporal and spatial resolution and multi-channel measurements from the Advanced Baseline Imager (ABI) on the next-generation series of Geostationary Operational Environmental Satellites (GOES-R) are ideal for assisting these smaller, stand-alone radiometers. Based on sensitivity tests, the water vapor retrievals from TEMPEST are improved by adding water-vapor-sounding channels at 6.2, 6.9, and 7.3 mm from ABI, which help to increase the vertical resolution of soundings and reduce retrieval errors. Under clear sky conditions, retrieval biases and root-mean-square errors improve by approximately 10 %, while under cloudy skies, biases remain unchanged, but root-mean-square errors still decrease by 5 %. Humidity soundings are also validated using coastal radiosonde data from the Integrated Global Radiosonde Archive (IGRA) from 2019 to 2020. When ABI indicates clear skies, water vapor retrievals improve somewhat by decreasing the overall bias in the microwave only estimate by roughly 10 %, although layer root-mean-square errors remain roughly unchanged at 1 g/kg when three ABI channels are added. When ABI indicates cloudy conditions, there is little change in the results. The small number of matched radiosondes may limit the observed improvement.

1. Introduction

The Temporal Experiment for Storms and Tropical Systems Demonstration (TEMPEST-D; Reising et al., 2018) mission was designed to demonstrate the capability of a small radiometer on board a 6U CubeSat satellite for deriving clouds, water vapor, and precipitation. The CubeSat, including the flight system and the TEMPEST-D radiometer, is 10 cm x 20 cm x 34 cm and weighs 11.2 kg. Although the size of the TEMPEST-D is much smaller than instruments such as the operational Microwave Humidity Sounders (MHS on NOAA-18/19 and MetOp-A/B/C), which weigh about 63 kg, the TEMPEST-D radiometer demonstrated the capability to provide comparable well-calibrated microwave (MW) measurements (Berg et al., 2021; Brown et al., 2023). In addition, Schulte et al. (2020) introduced the bias correction of Earth incidence angle (EIA) (Schulte and Kummerow, 2019) in the Optimal Estimation (OE; Rodgers, 2000) framework with TEMPEST-D and demonstrated the potential of getting consistent retrievals from a fleet of TEMPEST sensors observing the same spot with different EIAs. Radhakrishnan et al. (2022) estimated surface rainfall by machine-learning methods and showed that retrieved rainfall using TEMPEST-D channels was consistent with the multi-radar/multi-sensor system (MRMS) rainfall products over the Continental United States. The success of TEMPEST-D led to flying a second TEMPEST

44   unit in conjunction with the Compact Ocean Wind Vector Radiometer (COWVR;
45   https://podaac.jpl.nasa.gov/COWVR-TEMPEST) currently in orbit aboard the International Space
46   Station.
47
48   Several studies have shown the capability of retrieving surface and atmospheric variables over the
49   ocean under non-raining conditions using Optimal Estimation (OE) techniques. Elsaesser and
50   Kummerow (2008) retrieved total precipitable water (TPW), surface wind, and cloud liquid water path
51   (CLWP) using observations from the Advanced Microwave Scanning Radiometer-Earth Observing
52   System (AMSR-E), the Special Sensor Microwave/Imager (SSM/I), and the Tropical Rainfall Measuring
53   Mission (TRMM) Microwave Imager (TMI) using the same OE configurations. This was later expanded
54   to the Global Precipitation Measurement (GPM) Microwave Imager (GMI) (Duncan and Kummerow,
55   2016). The Colorado State University 1 D variational inversion algorithm (CSU 1DVAR) has been
56   validated by comparing results with other independent products, showing that CSU 1DVAR can provide
57   consistent results across a broad spectrum of sensors (Elsaesser and Kummerow, 2008; Duncan and
58   Kummerow, 2016; Schulte and Kummerow, 2019; Schulte et al., 2020). A conceptually similar OE
59   method is employed in the Microwave Integrated Retrieval System (MiRS; Boukabara et al., 2011,
60   2013, 2018) designed to provide various atmospheric and surface parameters (skin temperature,
61   surface emissivity, and profiles of temperature, water vapor, non-precipitating clouds, and
62   precipitations) under all sky conditions over ocean and land surfaces. Due to its flexible structure, MiRS
63   is used operationally at NOAA and supports measurements from multiple MW instruments, including
64   the TMI, GMI, MHS, Atmospheric Microwave Sounding Unit (AMSU), SSM/I, Special Sensor Microwave
65   Imager/Sounder (SSMI/S), and Advanced Technology Microwave Sounder (ATMS).
66
67   Infrared (IR) sounders, and especially hyperspectral IR sounders, while limited to clear sky conditions,
68   have distinct advantages for deriving temperature and moisture profiles due to their sharper weighting
69   functions, particularly in the upper troposphere when no clouds are present. Using MW measurements
70   from AMSU-A and MHS plus IR observations from the Infrared Atmospheric Sounding Interferometer
71   (IASI) on board the MetOp platforms, Aires (2011) and Aires et al. (2011, 2012) significantly reduced
72   the errors of retrieving temperature and water vapor profiles under clear sky conditions over the
73   ocean by comparing with retrievals using individual MW or IR instruments alone. Under the European
74   Space Agency Water Vapour Climate Change Initiative project (Siddans et al., 2015; Siddans, 2019),
75   Trent et al. (2023) validated 9.5 years of atmospheric profiles retrieved from MetOp MW and IR
76   observations and showed that global biases of temperature and water vapor are within 0.5 K and 10 %,
77   respectively, making the retrieval products an important climate data record.
78
79   In addition to MW and IR measurements on the MetOp platforms, Milstein and Blackwell (2016) also
80   showed the advantages of using MW and IR spectral bands from the Atmospheric Infrared Sounder
81   (AIRS) and AMSU on the Aqua satellite as well as from the Cross-Track Infrared Sounder (CrIS) and
82   ATMS on the Suomi National Polar-orbiting Partnership satellite (Suomi NPP) for temperature and
83   water vapor retrievals. The NOAA Unique CrIS/ATMS Processing System (NUCAPS; Gambacorta et al.,
84   2012) was built specifically to retrieve global atmospheric profiles using MW sensors (AMSU, ATMS,
85   and MHS) and hyperspectral IR instruments (AIRS, CrIS, or IASI) under non-precipitating conditions with
86   up to 80 % effective cloud fraction. Sun et al. (2017) used radiosonde data to assess the sounding
87   products from NUCAPS, indicating small biases in the lower atmosphere for temperature profiles of

88 less than 0.5 K and less than 20 % for water vapor profiles. These profiles have been further improved
89 by Ma et al. (2021), who applied a neural network technique to enhance the retrieved atmospheric
90 profiles in NUCAPS products by using IR channels on the next-generation series of Geostationary
91 Operational Environmental Satellites (GOES-R; Schmit et al., 2008). The root-mean-square error of
92 retrieved temperature and humidity profiles in that study decreased by more than 30 % from the
93 surface up to 700 hPa. Thus, while it seems clear from these previous studies that merging IR and MW
94 soundings from the same platforms is beneficial, CubeSat sounders such as TEMPEST or the Time-
95 Resolved Observations of Precipitation structure and storm Intensity with a Constellation of Smallsats
96 (TROPICS; Blackwell et al., 2018) do not generally fly in tandem with hyperspectral IR sounders. In this
97 case, it is useful to examine if there are benefits to merging the stand-alone passive MW sensors with
98 geostationary IR-sounding channels.
99
100 The Advanced Baseline Imager (ABI), on board the GOES-R satellite series, observes the full disk of the
101 Earth every 10 minutes (15 minutes prior to April 2019), measuring in the visible (VIS), near-IR, and IR
102 spectral bands with spatial resolutions from 0.5 to 2 km. Three water vapor channels at (6.2, 6.9, and
103 7.3 mm) make ABI suitable for deriving water vapor profiles with similar vertical resolution to the
104 operational MW sensors (Schmit et al., 2008; Li et al., 2019). Due to the high spatial and temporal
105 resolutions from GOES-R ABI observations over large regions, the ABI sensor can always be matched
106 with stand-alone MW radiometers over the sensed hemisphere, as illustrated by Ma et al. (2021). This
107 study thus focuses on the enhancement in water vapor retrievals that may be achieved when ABI IR
108 water vapor sounding channels are added to the TEMPEST-D MW channels.
109
110 **2.   Data**
111
112 The TEMPEST-D satellite (Reising et al., 2018) was deployed from the International Space Station on
113 July 13, 2018, into the Low Earth Orbit. The initial orbit height was 400 km with a 51.6° inclination,
114 observing an 825 km wide swath from the initial height. The mission successfully demonstrated both
115 the maneuverability of CubeSats to fly in closely maintained formations as well as the calibration
116 stability of the MW radiometer (Berg et al., 2021). The TEMPEST-D passive MW radiometer scanned
117 Earth in a cross-track mode and measured five channels at 87, 164, 174, 178, and 181 GHz with quasi-
118 horizontal polarization, except for 87 GHz, which measured quasi-vertical polarization. The spatial
119 resolutions of TEMPEST-D at the nadir were 14 km at 164 to 181 GHz and 28 km at 87 GHz. While the
120 data is not complete due to difficulties with the data receiving station at Wallops Island, Virginia, USA,
121 all available TEMPEST-D datasets can be requested through the website https://tempest.colostate.edu.
122 TEMPEST-D was deorbited on June 22, 2021. A second copy of TEMPEST was launched on Dec. 21,
123 2021, and is operating on the International Space Station in conjunction with COWVR. Data is available
124 from the National Aeronautics and Space Administration (NASA) Physical Oceanography Distributed
125 Active Archive Center (PODAAC) housed at NASA's Jet Propulsion Laboratory. Because the instruments
126 and orbits are identical, the results presented here apply to both sensors.
127
128 The GOES-16 (Schmit et al., 2008; Li et al., 2019) is the first of the GOES-R series satellites and was
129 launched on November 19, 2016, carrying several instruments, including ABI. GOES-16 replaces GOES-
130 13 and is located at longitude 75.2°W in a geostationary orbit (35786 km altitude), observing from
131 latitude 81.32°N to 81.32°S and from longitude 156.30°W to 6.30°E. This covers North and South

132   America, the eastern Pacific Ocean, and the Atlantic Ocean to the west coast of Africa. The ABI sensor
133   measures 16 spectral channels from VIS to IR bands (0.47 to 13.3 μm) with spatial resolutions ranging
134   from 0.5 km at 0.64 μm to 2.0 km in the IR. Only the three ABI-sounding channels at 6.2, 6.9, and 7.3
135   μm are used to enhance the TEMPEST-D retrieved water vapor profiles. While the ABI window and CO_2
136   channels add information, these channels have information that is largely redundant with the
137   TEMPEST window channels. To ensure spatial consistency between TEMPEST-D and the GOES-16, ABI
138   full disk products, all Radiances (RadF), Clear Sky Masks (ACMF), Cloud Top Phase (ACTPF), and Cloud
139   Top Pressure (CTPF) products from ABI, are averaged to match the 28 km TEMPEST-D horizontal
140   resolution and appended to TEMPEST-D observation locations and times. The GOES-16 products can be
141   downloaded through the Comprehensive Large Array Data Stewardship System (CLASS). Although
142   GOES-17 also covers parts of the TEMPEST-D operational period, its products are not used to avoid all
143   issues related to the cooling system, as described in https://www.goes-r.gov/users/GOES-17-ABI-
144   Performance.html.
145
146   Except for satellite observations and products mentioned above, auxiliary data, including surface wind
147   speed and direction, surface pressure, surface skin temperature, and temperature profiles, are also
148   used to constrain the retrievals. These are taken from the ERA5 (Hersbach et al., 2020), accessed
149   through the website https://www.ecmwf.int/en/forecasts/dataset/ecmwf-reanalysis-v5. The hourly
150   ERA5 data used in the study are 0.5° x 0.5° with 27 pressure levels from 1000 to 100 hPa. The vertical
151   resolution (in pressure coordinates) consists of 25 hPa intervals from 1000 to 750 hPa, 50 hPa intervals
152   from 750 to 250 hPa, and 25 hPa intervals from 250 to 100 hPa. One hour temporal resolution and 0.5°
153   spatial resolution from ERA5 is used to define unobserved surface conditions as well as the
154   temperature profiles. The auxiliary surface parameters and temperature profiles are linearly
155   interpolated in space and time to match the TEMPEST-D observations. The interpolated ERA5 auxiliary
156   data may not reflect the actual conditions at the satellite overpass location and time, so when
157   compared with in situ measurements, retrievals may be degraded by using the non-representative
158   auxiliary data.
159
160   3.   Methods
161
162   In satellite remote sensing, OE is a widely utilized technique to retrieve atmospheric components
163   (Rodgers, 2000; Elsaesser and Kummerow, 2008; Boukabara et al., 2011; Siddans et al., 2015; Duncan
164   and Kummerow, 2016; Schulte and Kummerow, 2019; Schulte et al., 2020). In OE, the state parameters
165   and measurement errors are all assumed to follow a Gaussian distribution, and the atmospheric states
166   being retrieved, x, are optimally estimated by minimizing the cost function J,
167
168    $$J = (x - x_a)^T S_a^{-1} (x - x_a) + [y - f(x)]^T S_y^{-1} [y - f(x)], \hspace{2cm} (1)$$
169
170   where x_a is the a priori information about the state vector x, y is the measurement vector, $f(x)$ is a
171   forward model simulating measurements for a given state x, S_a is the covariance matrix of a priori, and
172   S_y is the covariance matrix of measurement errors (Rodgers, 2000). The minimization of J is achieved
173   by iteratively solving for the state vector x using the Gauss-Newton method. Following Eq. 5.29 in
174   Rodgers (2000), the convergence criteria are achieved when
175

176 $$d_i^2 = (x_i - x_{i+1})^T \hat{S}^{-1}(x_i - x_{i+1}) \ll n, \tag{2}$$
177

178 where d measures the change in the state vector between ith and ith $+ 1$ iteration, and n is the
179 number of retrieved variables (levels of water vapor and/or layers of clouds in this study). The solution
180 is said to have converged when the residual is one tenth the number of the retrieved variables in the
181 study. This is consistent with the definition from Eq. (2) that the error weighted increment is much less
182 than the number of the retrieved variables. The a priori state vector x_a is used as the initial guess at
183 the beginning of the iteration. The a priori information x_a and its uncertainty S_a are derived from
184 monthly ERA5 humidity and cloud profiles over the ocean; x_a describes the mean state of the profiles,
185 and S_a accounts for the variation of the states. If sky conditions are known from GOES-16 cloud masks,
186 x_a and S_a obtained from clear or cloudy conditions will be used in the retrievals, or otherwise, a priori
187 values computed from all-sky conditions will be used.
188

189 The state vector x comprises the water vapor mixing ratio at different pressure levels and/or clouds.
190 The number of selected water vapor levels depends on the number of channels and the assumptions of
191 clouds. The selected water vapor levels are evenly distributed in pressure levels at 1000, 900, 800, 600,
192 and 400 hPa for TEMPEST only, and 1000, 950, 875, 800, 700, 600, 450, and 350 hPa when both
193 TEMPEST and ABI channels are used. The remaining water vapor levels are linearly interpolated.
194 Following previous studies (Schulte and Kummerow, 2019; Schulte et al., 2020), clouds are inserted
195 into single layers containing liquid and/or ice clouds in the profiles. Since passive MW sensors do not
196 have information about cloud top height, if clouds are assumed to be present, the state vector will
197 contain one layer of liquid and one layer of ice clouds with liquid cloud top at 900 hPa and ice cloud top
198 at 300 hPa. If cloud information is available from GOES-16 products, liquid clouds and/or ice clouds can
199 also be inserted following GOES-16 cloud information as listed in Table 1. The table allows for
200 experiments where the GOES-16 is used simply to determine if there are clouds in the field of view
201 (FOV) or the actual cloud properties. If GOES-16 is only used to make the clear or cloudy
202 determination, then the cloud fraction is set to 0 or 1, respectively. TEMPEST-D, by itself, has no ability
203 to retrieve the cloud fraction. If details of the cloud field are used, the cloud fraction is set accordingly.
204
205

206 Table 1. The retrieval configurations under clear and cloudy conditions with and without GOES-16
207 cloud information. CF, CH, and CP represent cloud fraction, cloud height, and cloud phase, respectively.
208

Sensors	Using GOES-16 cloud products	
	Clear sky	Cloudy sky
TEMPEST+ABI (8 channels) or TEMPEST (5 channels)	1. No, set CF to 1 2. Yes, set CF to 0	1. No, set CF to 1 2. Yes, set CF from GOES-16 3. Yes, set CF, CH, and CP from GOES-16

209
210

211 The measurement error covariance matrix S_y is derived from two uncertainty sources: the radiometer
212 and the forward model (Elsaesser and Kummerow, 2008; Duncan and Kummerow, 2016; Schulte and
213 Kummerow, 2019; Schulte et al., 2020). The noise equivalent differential temperature (NEDT) values

214   are represented as the radiometer measurement errors for each sensor channel. For TEMPEST from 87
215   to 181 GHz, the NEDT values are 0.20, 0.35, 0.55, 0.55, and 0.75 K, respectively, which are evaluated
216   between 275 and 315 K (Berg et al., 2021; Padmanabhan et al., 2021). The NEDT values of ABI are 0.1 K
217   for all ABI IR channels, except for band 16, which is 0.3 K, and are evaluated at 300 K (Goodman et al.,
218   2019; GOES-R Series, 2022). The forward model uncertainties are approximated by comparing
219   simulated satellite observations using full ERA5 profiles to degraded simulated measurements using
220   the assumptions made in the OE retrievals, as described above. While the radiative transfer model is
221   assumed to contain no errors, errors are introduced when complex water vapor profiles are replaced
222   by simplified water vapor profiles at the prescribed levels, and complex cloud vertical profiles are
223   replaced by single liquid and ice cloud layers containing the equivalent cloud water path. The
224   measurement error covariance matrix S_y is then derived from the NEDT values and the estimated
225   forward model errors. Figures 1(a), 1(b), and 1(c) show the S_y estimated from all, cloudy and clear
226   skies, respectively, based on oceanic ERA5 profiles. Since ERA5 profiles most often contain some
227   degree of clouds, Figs. 1(a) and 1(b) have similar patterns, and channels having similar water vapor
228   sensitivity are more correlated with each other. On the other hand, due to much lower atmospheric
229   absorption in the clear skies, the surface-sensitive TEMPEST channels (87 and 164 GHz) have higher
230   correlations among themselves as in Fig. 1(c), although with smaller overall S_y values than in Figs. 1(a)
231   and 1(b).
232
233
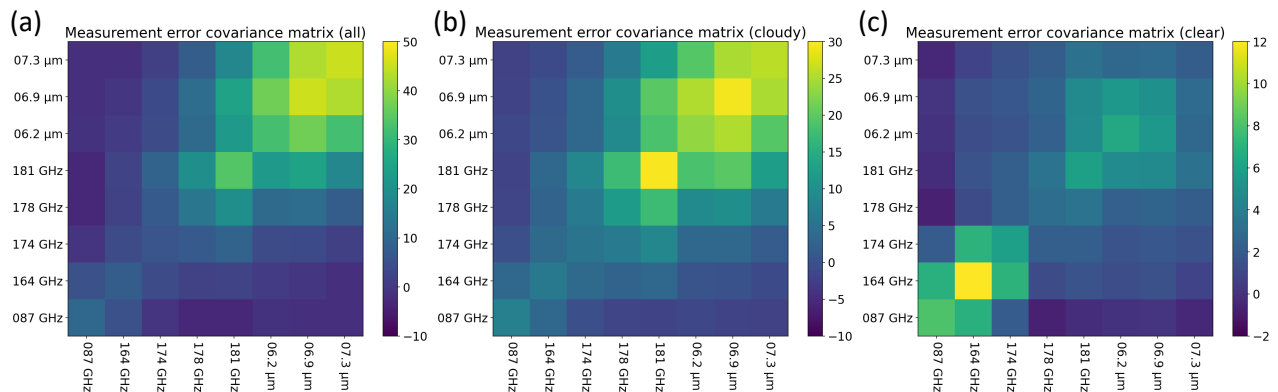
235   Figure 1. Measurement error covariance matrix S_y for five TEMPEST-D MW and three ABI IR channels
236   derived from ERA5 profiles under (a) all sky, (b) cloudy sky, and (c) clear sky conditions over the ocean.
237
238
239   The forward model is composed of two radiative transfer models: one simulates MW observations, and
240   the other computes IR measurements. In the study, the Community Radiative Transfer Model (CRTM;
241   Liu et al., 2012; Johnson et al., 2023) version 2.3.0 is used to calculate the observed brightness
242   temperature for the ABI IR channels. The model can be downloaded through the website
243   https://github.com/JCSDA/crtm. To simulate TEMPEST MW observations, an Eddington approximation,
244   as described in Schulte and Kummerow (2019) and Schulte et al. (2020), is used. The Monochromatic
245   Radiative Transfer Model (MonoRTM; https://github.com/AER-RC/monoRTM; Clough et al., 2005) is
246   used to generate the atmospheric absorption while the ocean surface MW emissivity is computed
247   using the FAST microwave Emissivity Model version 6 (FASTEM-6; Kazumori and English, 2015). Clouds

248 are assumed to be homogeneously distributed in single layers. The cloud top pressure is 900 hPa for
249 liquid clouds and 300 hPa for ice clouds if no cloud top heights are assigned from GOES-16 products, as
250 described earlier. The MW optical properties of liquid clouds are generated by Lorenz-Mie theory (van
251 de Hulst, 1957; Bohren and Huffman, 1998), assuming the droplet is spherical with a radius of 12 μm
252 and is monodisperse in particle size distribution (PSD). The radiative properties of ice clouds in the MW
253 spectrum are computed using the single-scattering property databases for non-spherical ice particles
254 from Liu (2008) and Nowell et al. (2013) following the analysis of Schulte and Kummerow (2019). The
255 databases are derived by the discrete-dipole approximation method (Draine and Flatau, 1994). The
256 microphysical properties of ice clouds used to derive the scattering properties are assumed to have the
257 PSD from Field et al. (2007) with a constant density of 100 g/cm^3 and have ice habits: 6 bullet rosettes
258 (crystal size < 800 μm) and aggregates of 400 μm rosettes (crystal size ≥ 800 μm). Ice clouds can be
259 one of the major error sources in radiative transfer simulations (Kulie et al., 2010; Ringerud et al.,
260 2019; Schulte and Kummerow, 2019), but are not considered here.
261
262 The monthly means and variability of water vapor mixing ratios from ERA5 above 200 hPa are
263 extremely small, as shown in Fig. 2. The sensor responses to these small amounts of stratospheric
264 water vapor are less than the noise of 0.2 to 0.75 K for TEMPEST and 0.1 to 0.3 K for ABI. Therefore,
265 the water vapor mixing ratio was set to the monthly mean climatology above 200 hPa and is not
266 retrieved explicitly with the available channels.
267
268
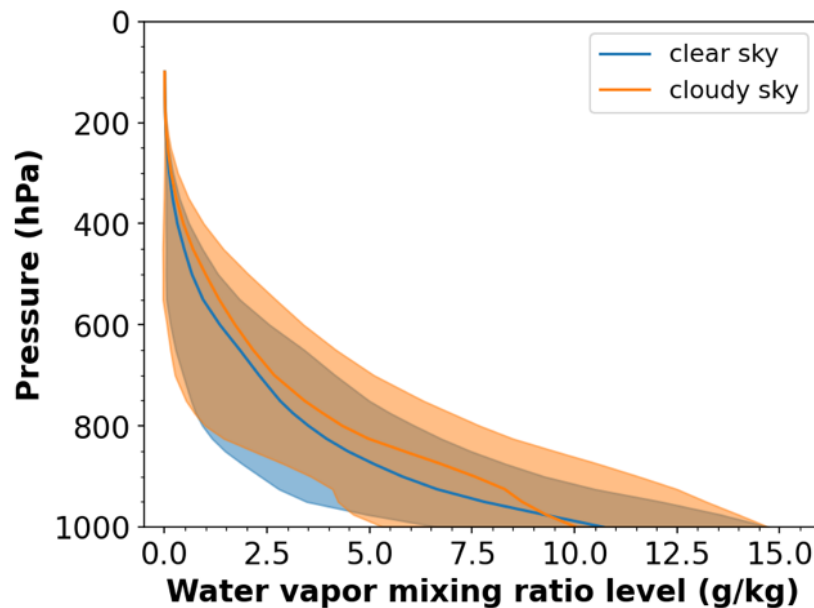
269
270 Figure 2. Monthly mean and standard deviation (σ) of water vapor profiles under clear and cloudy
271 conditions over the ocean between $\pm 60°$ latitudes from ERA5 in May 2020. Blue color represents
272 water vapor in clear skies, while orange color shows water vapor in cloudy skies. Solid lines are mean
273 water vapor profiles, and shaded areas are standard deviations.
274
275

276   With the model configuration described above and a priori atmospheric temperature and water vapor
277   profiles from ERA5 shown in Figs. 3(a) and 3(b), the sensitivity of water vapor to five TEMPEST-D MW
278   channels and three ABI IR bands is represented by the clear sky Jacobians shown in Fig. 3(c), and in the
279   cloudy sky Fig. 3(d) present the Jacobians of water vapor and clouds. For humidity, all TEMPEST MW
280   and ABI IR channels have different degrees of sensitivity along the altitude axis. In clear or cloudy skies,
281   three ABI water-vapor-sounding channels only provide signals for the upper atmosphere. However,
282   under the same conditions, signals of water vapor are sensed by the TEMPEST MW bands from the
283   surface to the top of the atmosphere. TEMPEST 87 and 164 GHz spectral bands have significant
284   sensitivity to water vapor and liquid clouds through the entire lower atmosphere. Except for the
285   TEMPEST 87 GHz band, all remaining TEMPEST channels have sensitivity to ice clouds. Overall, as also
286   shown in the studies mentioned in the introduction (Aires, 2011; Milstein and Blackwell, 2016; Sun et
287   al., 2017; Ma et al., 2021; Trent et al., 2023), Figs. 3(c) and 3(d) demonstrate the advantage of merging
288   IR spectral and MW spectral bands in soundings: MW channels have humidity signals under cloudy
289   conditions, and IR bands provide extra information about the upper atmosphere.

290
291
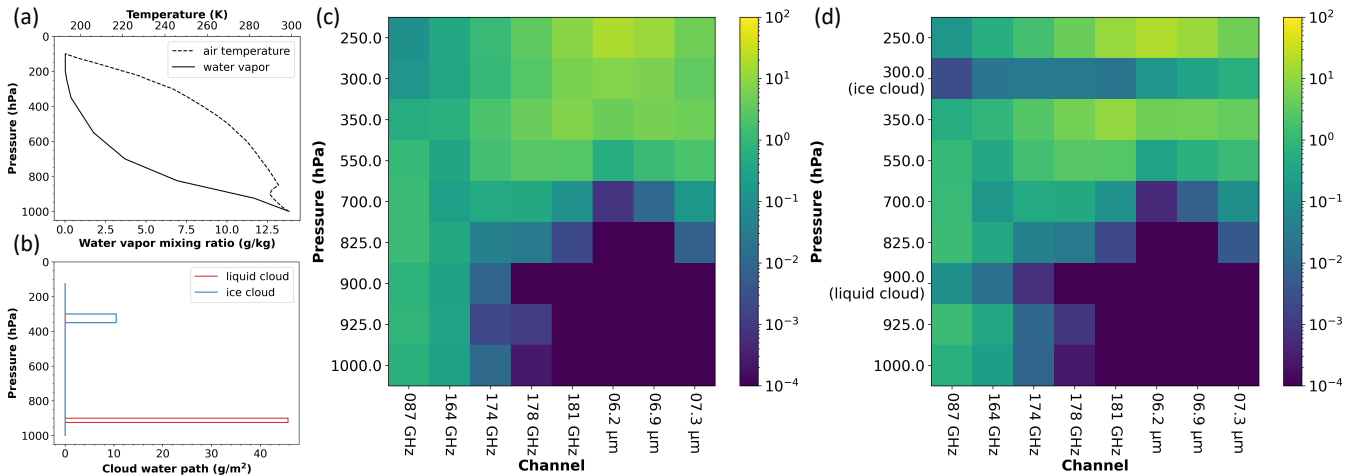
292
293   Figure 3. An example of water vapor and cloud Jacobians and the ERA5 profiles over the ocean used to
294   compute the Jacobians. (a) Profiles of air temperature and water vapor mixing ratio. (b) Liquid and ice
295   cloud layers. (c) Water vapor Jacobians from 250 to 1000 hPa in the clear sky as a function of sensor
296   channels (TEMPEST-D from 87 to 181 GHz and ABI from 6.2 to 7.3 μm). (d) The same as (c) but for
297   water vapor Jacobians from 250 to 1000 hPa and Jacobians of liquid (cloud top at 900 hPa) and ice
298   (cloud top at 300 hPa) clouds in the cloudy sky. The unit of the color for water vapor Jacobians is
299   K/g/kg, and for liquid and ice cloud Jacobians is K/g/m^2.

300
301
302   Given the frequent observation from GOES-R ABI, the data can be readily merged with TEMPEST-D.
303   Figure 4 shows the overlap of the two sensors over the ocean. Gaps between MW orbits, as well as
304   cloudy regions where ABI detects clouds, are evident in both images. Even though ABI cannot be used
305   for sounding in cloudy atmospheres, using the ABI cloud products can still provide retrievals some prior
306   knowledge about clouds (cloud fraction, phase, and height), which will be shown to positively impact
307   the TEMPEST-D MW retrievals. The next section will explore retrieval sensitivities under clear and

308 cloudy conditions using synthetic TEMPEST-D and ABI observations simulated from ERA5 profiles.
309 Retrieved water vapor profiles are then validated against in situ radiosonde humidity measurements
310 under different retrieval assumptions, as listed in Table 1.
311
312
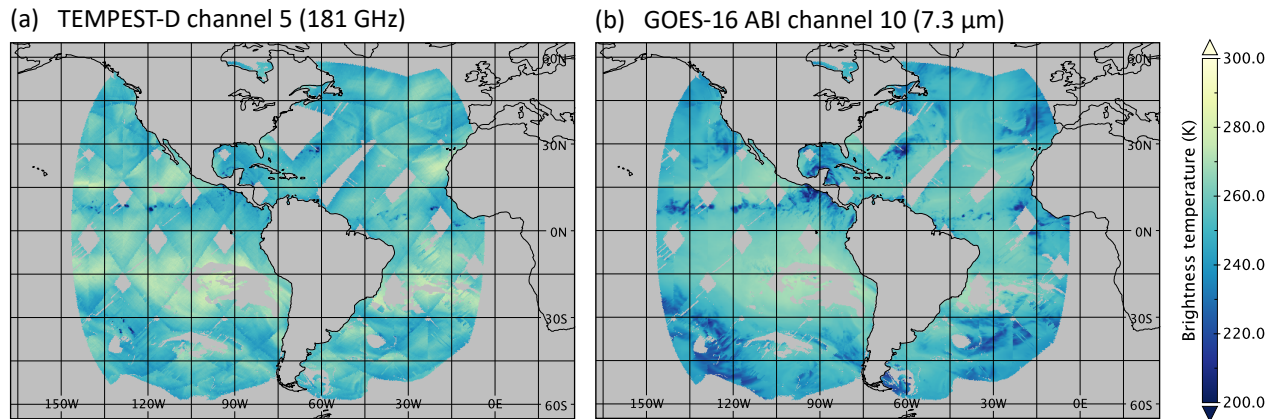
313
314 Figure 4. Collocated TEMPEST-D and GOES-16 ABI observations over the ocean on 2020/06/01 for (a)
315 TEMPEST-D channel 5 (181 GHz) and for (b) ABI channel 10 (7.3 µm).
316
317

4.   Results

4.1. Sensitivity Tests

Observations for the TEMPEST five (87, 164, 174, 178, and 181 GHz) and ABI three (6.2, 6.9, and 7.3
µm) channels are simulated using temperature, humidity, cloud profiles, surface temperature, and
surface wind speed and direction from ERA5 over the ocean with viewing angles corresponding to
TEMPEST and ABI instruments respectively. All data corresponds to May 27, 2020. Since the true states
from the ERA5 data are known, the retrieval accuracy can be evaluated using the computed observed
brightness temperature under different scenarios.

4.1.1. Case studies

Two cases are used to illustrate the humidity retrievals first using only the TEMPEST sensor and then
adding three ABI channels in clear and cloudy sky scenes. These are shown in Fig. 5. While the
retrieved profiles do not change dramatically, the additional ABI water-vapor-sounding channels can
be seen to improve the mid-tropospheric biases, as shown in Figs. 5(b) and 5(d) respectively. Although
the retrieved water vapor profiles are over- and under-estimated along the height when compared to
the true ERA5 values, Fig. 5 reveals that the retrievals using three extra ABI IR channels improve
significantly with respect to both bias and standard deviation above the 800 hPa level where the ABI
channels are expected to add the most information. While overall biases and standard deviations also
decrease for both examples, it is apparent that ABI has little influence over the low-level water vapor
and that most of the improvement actually comes from the mid to upper troposphere.

342
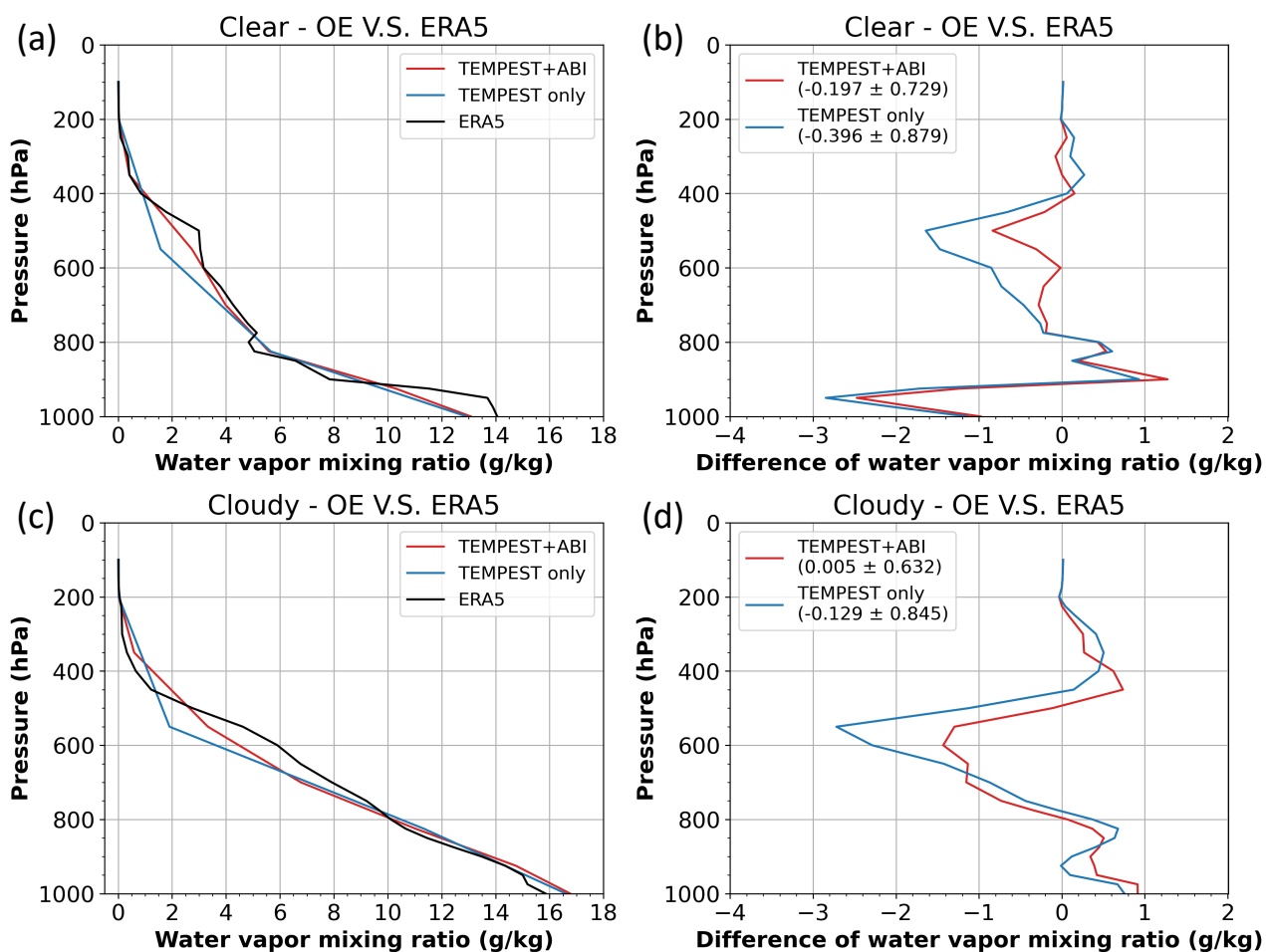
343
344 Figure 5. Selected cases of retrieved water vapor profiles using the synthetic observations from ERA5
345 over the ocean on 2020/05/27 and using all-sky a priori. Figures (a) and (b) show retrievals under clear
346 conditions, while cloudy retrievals are presented in Figures (c) and (d). Figures (a) and (c) show the
347 retrieved and ERA5 humidity profiles and the corresponding comparisons between retrievals and ERA5
348 (retrievals minus ERA5) are presented in Figures (b) and (d). The solid black lines are water vapor
349 profiles from ERA5. The solid red lines are water vapor retrievals using TEMPEST and ABI combined
350 channels, and the solid blue lines are retrievals using the TEMPEST sensor. The number in the
351 parentheses is the bias $\pm$ standard deviation of the whole profile.
352
353
354   **4.1.2. Statistics**
355
356 Comparisons of humidity retrievals using merged five TEMPEST MW bands and three ABI-sounding
357 channels (6.2, 6.9, and 7.3 μm) versus using only the TEMPEST sensor are performed for 1000
358 randomly selected clear or cloudy sky cases. Since in the observations on 2020/05/27, all clear sky
359 pixels are about 1200 samples and about 8400 cases are cloudy pixels according to the GOES-16 cloud
360 mask, randomly selecting 1000 pixels over clear and cloudy cases are for fair comparisons between
361 clear and cloudy statistics, which are about the same no matter how we randomly selected the 1000

362 clear or cloudy samples. Results in clear skies are shown in Fig. 6. As with the case studies, adding three
363 ABI channels clearly reduces layer biases and random errors in the retrieved water vapor profiles.
364 Errors in the retrieved water vapor above 800 hPa are significantly smaller when using the five MW
365 bands from TEMPEST in combination with the three ABI channels. While the overall water vapor biases
366 and standard deviations under clear conditions are reduced only slightly from (-0.149 $\pm$ 1.127 g/kg) for
367 TEMPEST only to (-0.128 $\pm$ 1.022 g/kg) for TEMPEST+ABI, much larger reductions can be seen in the
368 layer values shown in Fig. 6 – starting at 900 hPa and extending all the way to 300 hPa.
369
370
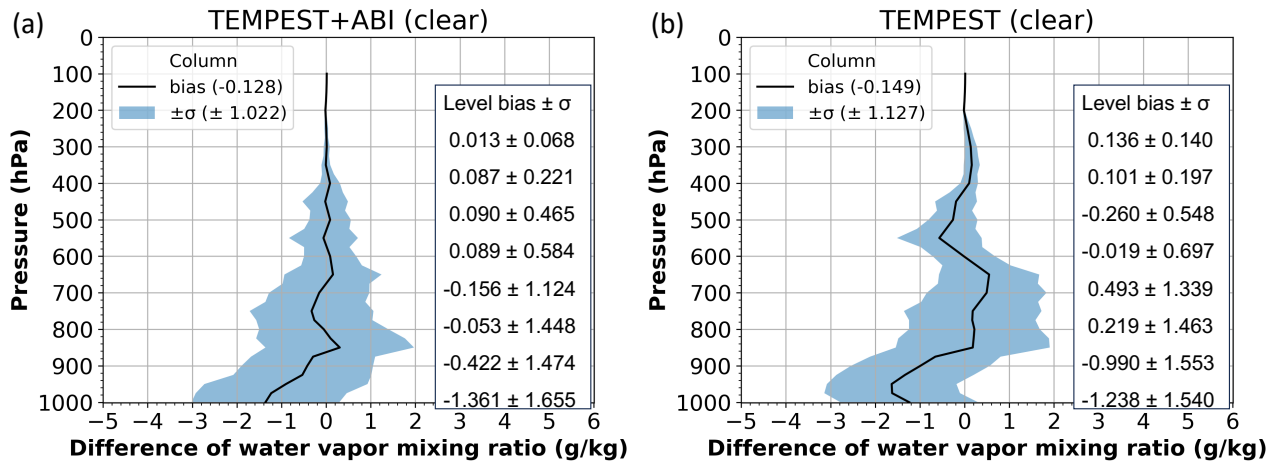
371
372 Figure 6. Sensitivity tests of retrieving water vapor profiles using the synthetic measurement from
373 ERA5 under clear conditions over the ocean on 2020/05/27 and using all-sky a priori. Figure (a) shows
374 retrievals using TEMPEST and ABI combined channels, and retrievals using only TEMPEST channels are
375 for Figure (b). Figures (a) and (b) show the difference in water vapor mixing ratio from 1000 randomly
376 selected profiles between retrievals and ERA5 (retrievals minus ERA5) along the height. The solid black
377 lines are the bias value, and the blue shade area is the standard deviation (σ). The included table
378 quantifies the retrieval performance from 300 to 1000 hPa for every 100 hPa.
379
380
381 Similarly, the accuracy of humidity retrievals from 1000 randomly selected cloudy cases using two
382 different sensor configurations is shown in Figs. 7(a) and 7(b). Consistent with the case study and clear
383 sky cases shown in Fig. 6, adding three ABI IR channels to the retrievals also reduces biases in the mid-
384 tropospheric layers for cloudy scenes. Due to the lack of sensitivity of three ABI-sounding channels to
385 the lower atmosphere, as shown in Figs. 3(c) and 3(d), the performance of water vapor retrievals
386 around the surface shows only a negligible improvement in both clear and cloudy skies. While the
387 column metrics show unbiased results with or without ABI, the standard deviation of retrieval errors is
388 larger when using TEMPEST-only retrievals (1.022 g/kg) than using merged TEMPEST and ABI channels
389 (0.949 g/kg). Quantitative comparisons of the vertical profiles in Figs. 7(a) and 7(b) again reveal that
390 the layer biases are significantly reduced in the TEMPEST+ABI retrievals relative to TEMPEST alone,
391 reducing the individual layer biases by approximately 50 % (although not uniformly in all layers). The
392 overall biases are smaller than in the clear case. The latter is explained by the fact that the all-sky a
393 priori guess comes from the climatology of ERA5 profiles for the month, and these profiles

394 overwhelmingly contain clouds. The cloudy retrieval is thus less biased in the initial iteration, while the
395 clear retrievals must adjust the first guess to correspond to drier conditions when the atmosphere is
396 cloud-free. Standard deviations are slightly larger for cloudy scenes, as should be expected from a
397 more complex retrieval.
398
399
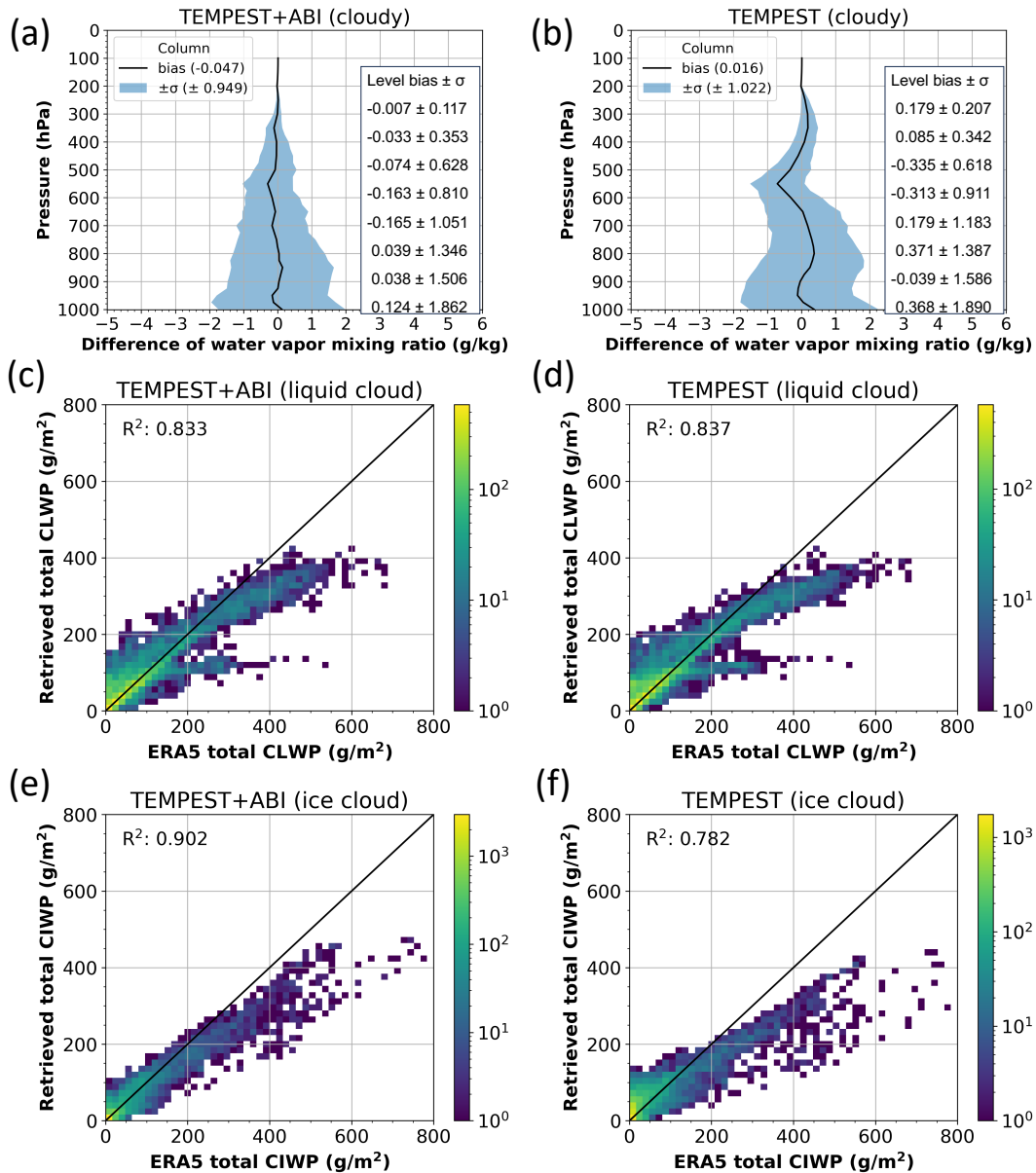
400
401 Figure 7. Sensitivity tests of retrievals of water vapor, liquid and ice clouds using synthetic observations
402 from ERA5 under cloudy conditions over the ocean on 2020/05/27 and using all-sky a priori. Figures (a),
403 (c), and (e) show retrievals using TEMPEST and ABI combined channels, and retrievals using only
404 TEMPEST channels are for Figures (b), (d), and (f). Figures (a) and (b) show the difference in water
405 vapor mixing ratio from 1000 randomly selected profiles between retrievals and ERA5 (retrievals minus
406 ERA5) along the height. The solid black lines are the bias value, and the blue shade area is the standard
407 deviation (σ). The included table quantifies the retrieval performance from 300 to 1000 hPa for every

100 hPa. Figures (c) and (d) are two-dimensional histograms of retrieved and ERA5 total cloud liquid water path from 8000 randomly selected cases (total number of cloudy pixels is about 8400). R^2 is the coefficient of determination. Color means the number of samples; the solid black lines are the one-to-one lines. Figures (e) and (f) are the same as Figures (c) and (d) but for the total cloud ice water path.

The performance of liquid and ice cloud retrievals is shown in Figs. 7(c) to 7(f). Compared with the cloud liquid water path from ERA5, the liquid cloud retrievals do not improve after incorporating three more ABI-sounding channels, shown in Figs. 7(c) and 7(d), as the cloud liquid water path signal is confined almost entirely to the 87 and 164 GHz channels of TEMPEST-D. The sensitivity to liquid clouds with and without ABI channels is similar, with R^2 values about 0.83. Since ice clouds are at a higher altitude and interact with the water-vapor-sounding channels, the 164 to 181 GHz TEMPEST and 6.2 to 7.3 μm ABI channels have different degrees of sensitivity, as shown in Fig. 3(d). Adding three ABI-sounding channels has larger impacts on the retrieved ice clouds, as the R^2 values increase from 0.782 using only TEMPEST bands to about 0.9 using eight combined channels from TEMPEST and ABI. Overall, the retrieved liquid and ice clouds are all underestimated compared with the ERA5 profiles. For liquid clouds, this is simply due to the saturation of the cloud water emission signal at roughly 300 to 400 g/m^2 with the available channels. For ice clouds, the primary signal is a brightness temperature depression due to scattering. While this signal does not saturate, thicker ice clouds (> 300 to 400 g/m^2) are often found in conjunction with liquid clouds in ERA5, leading to brightness temperature signatures that are more difficult to untangle.

4.2. Independent Validation

While the preceding section focused on synthetic brightness temperatures generated from ERA5 profiles, this section uses radiosonde data to validate retrievals from actual observations. The Integrated Global Radiosonde Archive (IGRA) has collected and quality-controlled in situ observations from over 2,800 global stations since 1905, providing vertical profiles of pressure, temperature, humidity, and wind speed and direction. The IGRA dataset can be accessed at https://www.ncei.noaa.gov/products/weather-balloon/integrated-global-radiosonde-archive. The IGRA dataset used in the study is version 2.2 and is collocated with TEMPEST-D and GOES-16 ABI observations from 2019 to 2020. To ensure consistency in collocated cases, the observations from these three datasets are all within 1 hour and 1 degree latitude/longitude. Because the OE retrieval discussed here is limited to oceans, the radiosondes used in this study are limited to coastal regions. To avoid surface contaminations, the collocated TEMPEST-D measurements are moved over the ocean to ensure that ~30 km (the sensor FOV) in all directions of the TEMPEST-D pixel is free of land. The displaced footprints must have the same cloud conditions (clear sky or cloudy) as determined by GOES-16 cloud products at the radiosonde location to ensure these locations are under similar atmospheric conditions. There are 19 collocated coastal IGRA stations in the GOES-16 FOV, as shown in Fig. 8. The collocated IGRA sites are around North America and the Caribbean Sea. Given GOES-16 cloud information, there are 104 collocated cases, of which 10 cases are cloud-free, and 94 cases are under different degrees of cloudy skies, as shown in Fig. 9. The limited number of coincident samples is due to infrequent TEMPEST-D overpasses coupled with infrequent (twice daily) radiosonde launches and

451 frequent data downlink problems of TEMPEST-D, leaving only this limited set of radiosondes to
452 compare to.
453
454
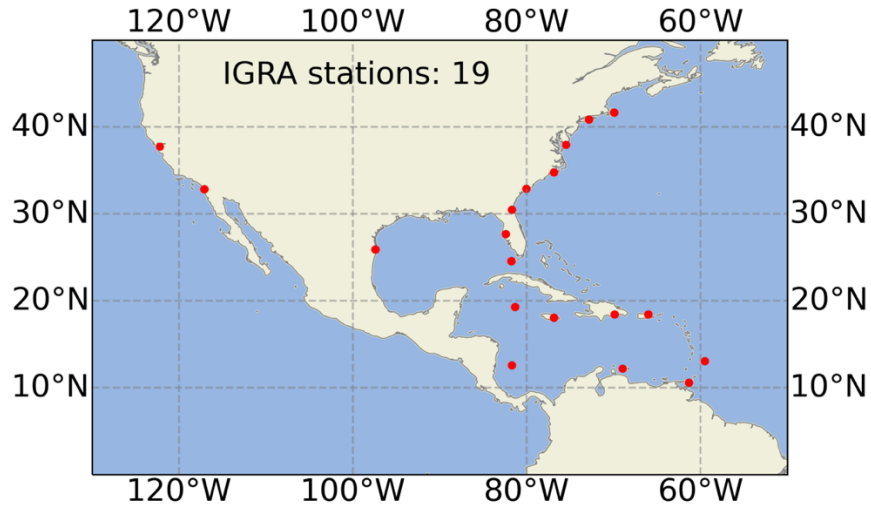
455
456 Figure 8. Map of collocated IGRA stations. The total number of collocated sites is 19, as marked in the
457 red circle dots.
458
459
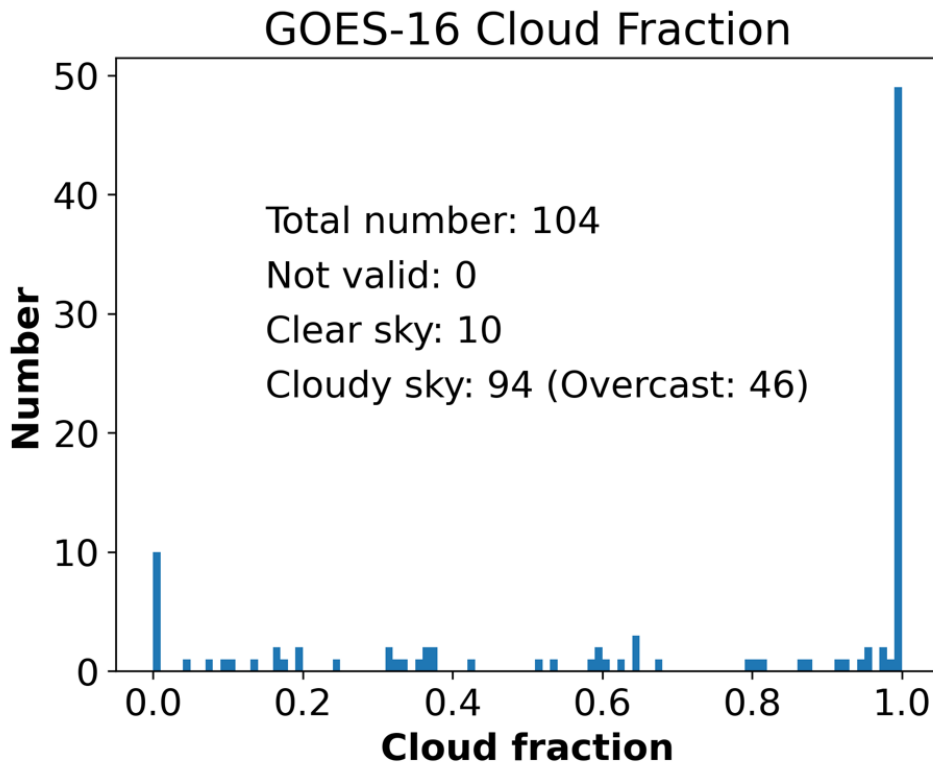
460
461 Figure 9. The histogram of GOES-16 derived cloud fraction at the collocated locations. The total
462 number of collocated cases is 104, including 10 clear and 94 cloudy cases.

463
464
465   With additional cloud information from GOES-16 products, water vapor retrievals are validated with
466   various levels of cloud information from the geostationary observations, as described in Table 1. The
467   most significant difference is that the algorithm does not retrieve clouds when the area is cloud-free
468   (as determined by ABI's cloud mask) and uses observations from all channels to retrieve water vapor
469   profiles only. Figure 10 shows the error in the retrieved water vapor profiles in clear skies, with biases
470   and standard deviations of column errors listed in Table 2. Only nine cases converged among ten clear
471   sky cases under four different retrieval settings. Experiments are performed with and without GOES-16
472   information. If GOES-16 cloud products are not used, the cloud fraction is set to 1.0, implying that
473   clouds covering the FOV are possible, although the retrieval can set the cloud water path to zero. The
474   convergence criteria from Eq. (2) are set to 0.8 for retrievals using TEMPEST-D and ABI eight channels
475   and are 0.5 for using TEMPEST-D five bands, as mentioned in section 3 (either 5 or 8 layers of
476   clouds/water vapor in this case).

477
478
479   Table 2. Compared with IGRA radiosonde observations, the column bias and standard deviation of
480   retrieved water vapor mixing ratio under the clear sky conditions. The statistic values are evaluated
481   based on all converged nine clear sky cases. CF means cloud fraction.
482

Sensors	Using GOES-16 cloud products	
	No set CF to 1	Yes set CF to 0
TEMPEST+ABI (8 channels)	-0.201 ± 1.029 g/kg	0.501 ± 1.071 g/kg
TEMPEST (5 channels)	-0.124 ± 1.156 g/kg	0.510 ± 1.078 g/kg

483
484
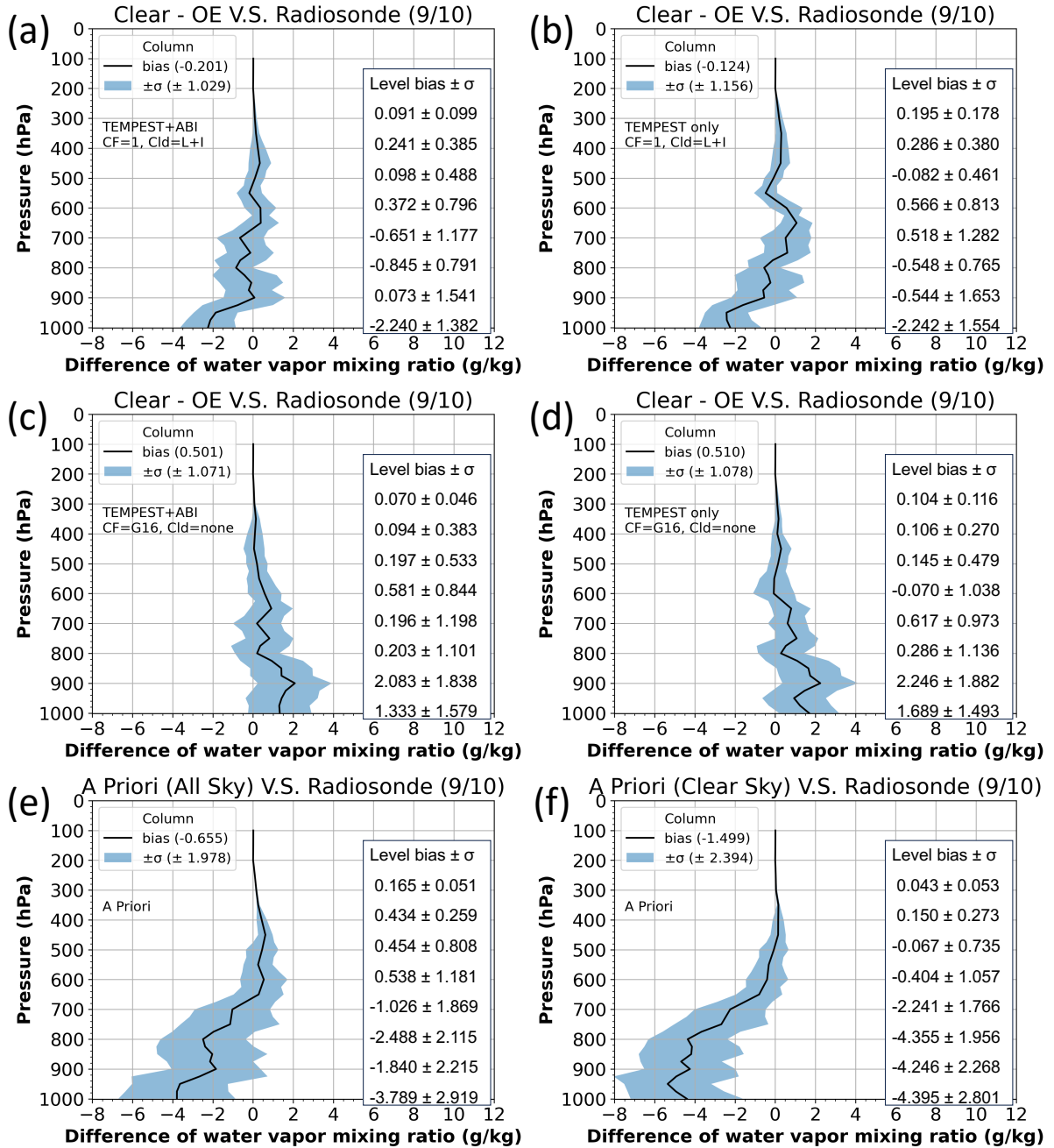
Figure 10. The water vapor mixing ratio difference between retrievals and radiosonde measurement (retrievals minus IGRA) in the GOES-16 observed clear skies. Retrievals use bands from TEMPEST-D and GOES-16 ABI in Figures (a) and (c) and use only TEMPEST-D channels in Figures (b) and (d). Retrievals in Figures (a) and (b) assume existing liquid and ice clouds with cloud fraction = 1 and use all-sky a priori, and retrievals in Figures (c) and (d) set no clouds with cloud fraction = 0 and use clear sky a priori. In the retrievals, the biases of the water vapor a priori information derived from all-sky conditions are shown in Figure (e), and obtained from clear skies are presented in Figure (f). The solid black lines are the bias value, and the blue shade regions indicate the standard deviation (σ). The included table quantifies the retrieval performance from 300 to 1000 hPa for every 100 hPa. The number in the

495   parentheses indicates the number of all converged cases out of all clear sky cases. G16 means GOES-16
496   products, and L+I indicates liquid and ice clouds.

497

498

499   The three additional water-vapor-sounding channels from ABI help to constrain water vapor profiles,
500   as shown in the reduced column error standard deviations as well as the layer biases and standard
501   deviations, although the differences are smaller than they were with the simulated results. Compared
502   with TEMPEST-only (Figs. 10(b) and 10(d)), the retrieved water vapor profiles above 800 hPa are visibly
503   less biased after including ABI channels (Figs. 10(a) and 10(c)). The overall statistics are not as
504   impressive because much of the water vapor is in the 1000 to 800 hPa layer, which is not improved by
505   additional ABI channels. Figures 11(a) and 11(b) present the erroneous retrieved liquid and ice clouds
506   under the clear conditions corresponding to Figs. 10(a) and 10(b), respectively. No clouds are
507   estimated in retrievals in Figs. 10(c) and 10(d), as this information is taken from the IR channels.
508   Because parts of the water vapor signals are falsely attributed to clouds, retrieved water vapor profiles
509   are underestimated when clouds are derived, as in Figs. 10(a), 10(b), and 11. On the other hand,
510   retrieved water vapor profiles are overestimated in Figs. 10(c) and 10(d) when the scene is forced to be
511   cloud-free based on ABI information. We speculate that, as with the synthetic retrievals, the bias from
512   ERA5 information in Fig. 10(f) under clear sky assumptions is even larger than if all sky ERA5 a priori in
513   Fig. 10(e) is used. This leads to even larger biases in the initial iteration, which the retrievals can only
514   partially correct without adding small amounts of cloud water to the scene. Conversely, it is also
515   possible that the small number of cases (9) simply are not representative.

516

517
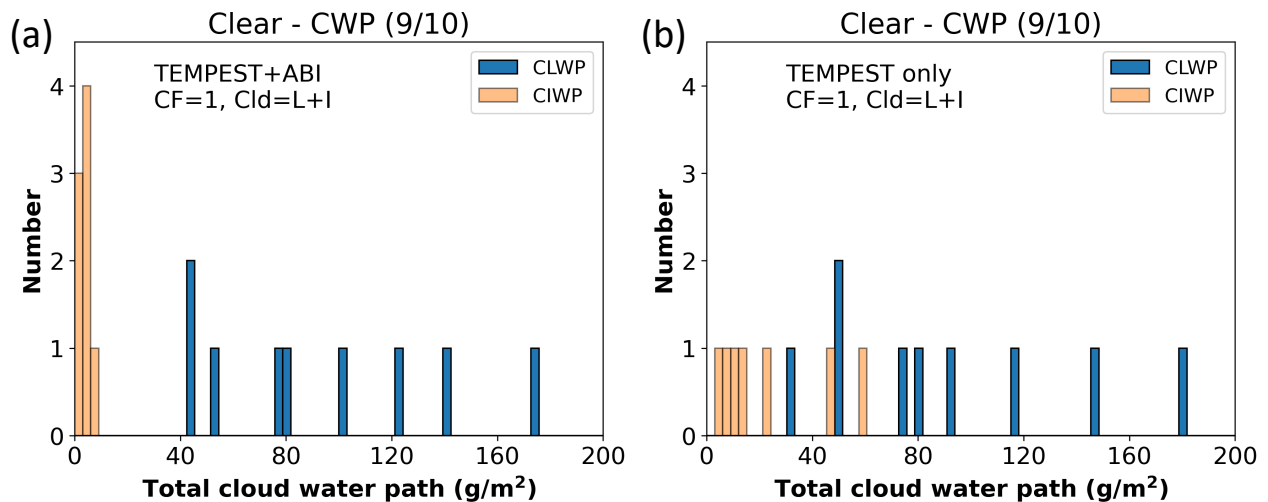
518
519   Figure 11. Retrieved total cloud water path for liquid and ice clouds in the clear sky cases with no cloud
520   information from GOES-16. Retrievals in Figure (a) use channels from TEMPEST-D and ABI and use only
521   TEMPEST-D channels for Figure (b). The number in the parentheses indicates the number of all
522   converged cases among all clear sky cases. L+I indicates liquid and ice clouds.

523

524

525 Water vapor retrieval errors under cloudy conditions for various assumptions of cloud knowledge are
526 presented in Fig. 12, with the corresponding bias and standard deviation of column errors listed in
527 Table 3. Although cases used in Table 3 and Figure 12 have all ABI and TEMPEST-D observations and all
528 cloud information, this is not the case for all other pixels. Therefore, Table 3 and Figure 12 show the
529 possible results from six different retrieval configurations using different degrees of cloud status and
530 using TEMPEST-only or with ABI measurements. The retrieval configurations in cloudy cases are listed
531 in Table 1. Retrievals in Figs. 12(a) and 12(b) have no information about clouds. In contrast, Figs. 12(c)
532 to 12(f) show results with different degrees of knowledge about clouds from ABI. Figures 12(c) and
533 12(d) use only cloud fractions. In the scenarios of no cloud information from ABI in Figs 12(a) and 12(b),
534 water vapor retrievals using TEMPEST+ABI have improvement above 500 hPa, between 700 and 800
535 hPa, and around the surface. When only cloud fraction is available from GOES-16 cloud products, Figs
536 12(c) and 12(d) show that adding ABI improves overall water vapor retrievals except for around 900
537 hPa. If the cloud fraction, cloud height, and cloud phase are all available from the cloud products as in
538 Figs 12(e) and 12(f), water vapor retrievals using ABI measurements have improvement around 300,
539 400, and 600 hPa and have minor or no improvement on the other levels. In general, when retrievals
540 use the same cloud status, column average water vapor retrieval biases using TEMPEST and ABI
541 observations are smaller than using TEMPEST-only measurements, as in comparisons with Figs 12(a)
542 and 12(b), Figs 12(c) and 12(d), and Figs 12(e) and 12(f). While column average water vapor retrievals
543 do not improve significantly by adding cloud fraction information, when cloud fractions are specified,
544 quantitative comparisons show some improvements between 500 and 700 hPa and around the surface
545 for TEMPEST+ABI retrievals in Figs. 12(a) and 12(c), and present some improvements above 400 hPa
546 and around 600 hPa and the surface for TEMPEST-only retrievals in Figs. 12(b) and 12(d). The water
547 vapor retrieval errors are further decomposed by cloud fraction from GOES-16, shown in Fig. 13, using
548 various retrieval configurations shown in Table 1 under cloudy conditions. Among six retrieval settings,
549 the estimated water vapor profiles are nearly unbiased when the cloud fraction is between 0.4 and 0.6
550 with about 0.5 g/kg of error standard deviation, as these amounts of clouds provide enough signals
551 and do not entirely obscure signals underneath. For low cloud fractions, assigning the cloud fraction
552 from GOES-16 ABI leads to a bias, although the standard deviation is roughly the same as if a cloud
553 fraction of 1 is assigned. This can be attributed to the nonlinear response of the MW radiances at 87
554 and 164 GHz to cloud water content. When the assigned cloud fraction is small, the retrieval must
555 assign all the necessary cloud liquid water to a small cloud fraction, saturating the radiance signals and
556 generally causing poorer retrievals. As was seen in the synthetic retrievals, saturation will cause the
557 cloud water to be underestimated, which will in turn lead to an overestimation in water vapor as the
558 OE tries to balance all radiance terms. If the scene is truly overcast (observed cloud fraction near 1.0),
559 there can be no difference between assigning a cloud fraction of 1.0 as the default assumption or 1.0
560 as an observed parameter, and this is reflected in the results as well.
561
562 Additional cloud information in the form of cloud fraction, cloud height, and cloud phase from GOES-16
563 products are shown in Figs. 12(e) and 12(f). When retrievals use more cloud information from GOES-16
564 (cloud fraction, height, and phase), water vapor retrieval biases shown in Fig. 12(e) are about half of
565 the biases in Figs. 12(a) and 12(c) around 600 hPa and shown in Fig. 12(f) are significantly improved
566 above 700 hPa except for around 600 hPa compared with 12(b) and 12(d), but lower layers in Fig. 12(e)
567 and 12(f) show larger biases and little difference between using only TEMPEST or TEMPEST+ABI. In
568 cloudy conditions, the only channels with sensitivity to the low-level water vapor are the TEMPEST 87

569 and 164 GHz channels, as shown in Fig. 3(d). However, some overfitting appears to be taking place. The
570 authors speculate that the ice scattering properties assumed in the retrieval's forward model may
571 cause excess depression at 87 and 164GHz channels, which in turn, requires the algorithm to increase
572 the cloud water and water vapor to match the brightness temperatures in those channels.
573
574 Table 3. Column bias and standard deviation of retrieved water vapor mixing ratio in the cloudy skies
575 when compared to IGRA radiosonde observations. Statistics are evaluated based on all converged 77
576 cloudy sky cases.
577

Sensors	Using GOES-16 cloud products		
	No set CF to 1	Yes set CF from GOES-16	Yes set CF, CH, and CP from GOES-16
TEMPEST+ABI (8 channels)	0.007 ± 1.440 g/kg	0.061 ± 1.462 g/kg	0.514 ± 1.665 g/kg
TEMPEST (5 channels)	0.039 ± 1.488 g/kg	0.083 ± 1.488 g/kg	0.575 ± 1.632 g/kg

578
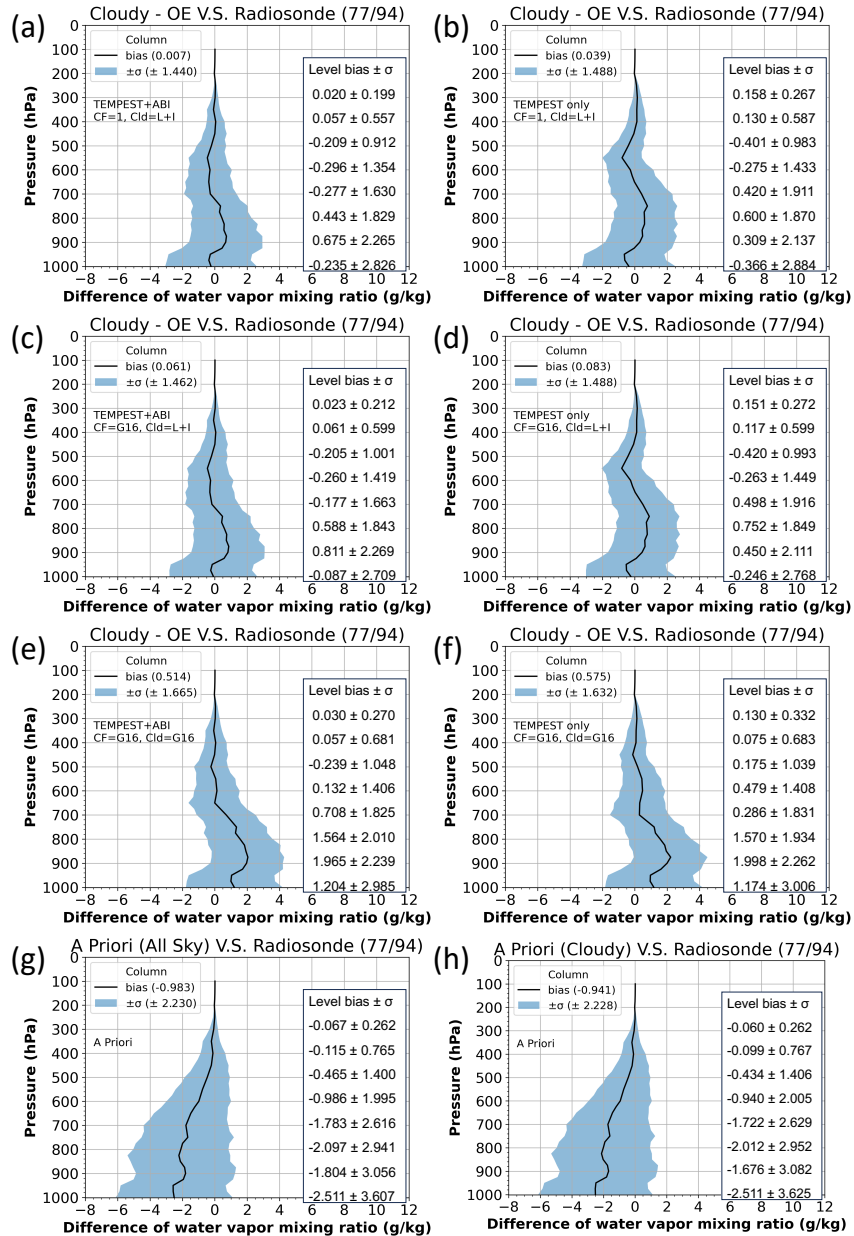
579
580 Figure 12. The water vapor mixing ratio difference between retrievals and radiosonde measurement
581 (retrievals minus IGRA) with GOES-16 observed cloudy conditions. Retrievals use bands from TEMPEST-
582 D and GOES-16 ABI in Figures (a), (c), and (e) and use only TEMPEST-D channels in Figures (b), (d), and
583 (f). Figures (a) to (d) show retrievals assuming liquid and ice clouds with cloud fraction = 1 for Figures
584 (a) and (b) and with cloud fraction from GOES-16 cloud mask for Figures (c) and (d). Retrievals in
585 Figures (e) and (f) use cloud fraction, height, and phase from GOES-16 products to define cloud layers.
586 Figures (a) and (b) use all-sky a priori, and Figures (c) to (f) use cloudy sky a priori. In the retrievals, the
587 biases of the water vapor a priori information derived from all-sky conditions are shown in Figure (g),
588 and obtained from cloudy skies are presented in Figure (h). The solid black lines are the bias value, and
589 the blue shade regions indicate the standard deviation (σ). The included table quantifies the retrieval
590 performance from 300 to 1000 hPa for every 100 hPa. The number in the parentheses means the

591 number of all converged cases out of all cloudy sky cases. G16 means GOES-16 products, and L+I
592 indicates liquid and ice clouds.
593
594
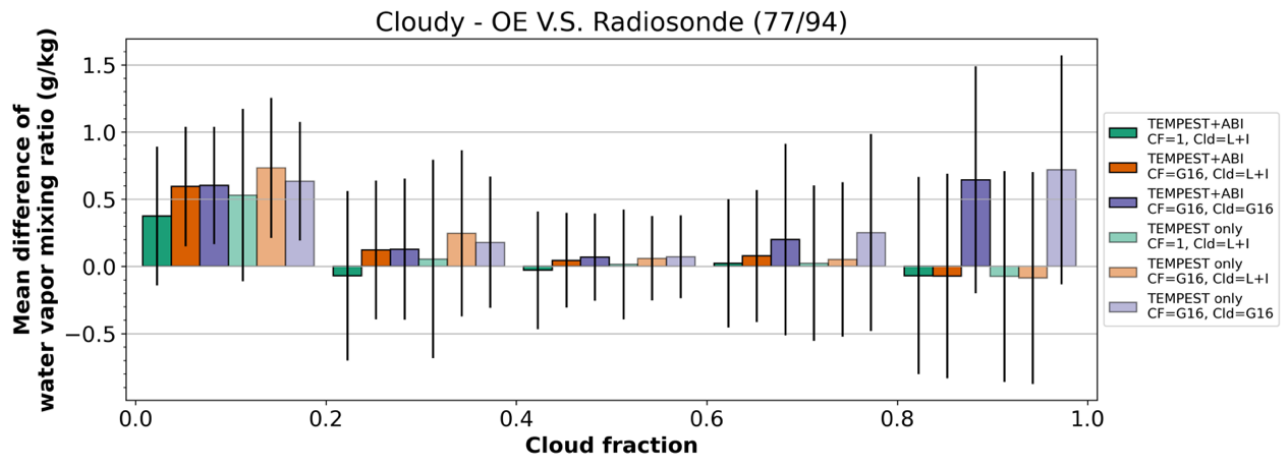
595
596 Figure 13. The mean difference between retrieved and radiosonde-observed water vapor profiles
597 (retrievals minus IGRA) within different GOES-16 cloud fraction intervals. Assuming both liquid and ice
598 clouds exist, the green bars indicate that retrievals use cloud fraction = 1, and the orange bars mean
599 that retrievals use only cloud fraction from GOES-16 products. The purple bars show retrievals using
600 cloud fraction, height, and phase from GOES-16 products. Lighter colors mean retrievals only use
601 TEMPEST-D, and darker colors show retrievals using both TEMPEST-D and GOES-16 ABI sensors. Solid
602 black lines are the range of $\pm$ standard deviation. The number in the parentheses means the number of
603 all converged cases among all cloudy sky cases. G16 means GOES-16 products, and L+I indicates liquid
604 and ice clouds.
605
606

5. Conclusions

608
609 TEMPEST-D successfully demonstrated the capability of CubeSats radiometers to maintain well-
610 calibrated MW signals in five channels from 87 to 181 GHz over a period of almost 3 years. Although
611 TEMPEST-D and the TEMPEST instrument currently flying with COWVR on the International Space
612 Station are economical and functional, these small MW radiometers fly without an accompanying
613 hyperspectral IR sensor typical on operational platforms. GOES-R ABI sensors provide observations of
614 the Earth every 1 to 10 minutes depending on the modes, and measure 16 spectral bands from VIS to
615 IR with 0.5 to 2.0 km ground resolution. Given such unique ABI observations with high spatial and
616 temporal resolution, supplemental information from ABI enhances the ability of TEMPEST as well as
617 other similar CubeSats to infer the states of the atmosphere.
618
619 Along with five TEMPEST MW bands, this study presented improvements in humidity profiles that are
620 possible when TEMPEST retrievals are supplemented with three IR water-vapor-sounding channels
621 available from GOES ABI. A number of positive outcomes were shown in this paper. In the sensitivity
622 tests comparing the combined MW/IR retrievals to MW-only capabilities, the effective vertical
623 resolution increases, as seen by smaller layer errors, under both clear and cloudy conditions. The

retrieved water vapor profiles were validated using independent IGRA humidity-sounding data from 2019 to 2020. During these two years of routine TEMPEST-D operations, only 104 IGRA cases (10 cases are clear scenes, 94 under different cloudy conditions) exist. Consistent with the sensitivity tests, the validation also showed the advantages of using GOES-16 cloud products and three additional ABI IR channels in water vapor sounding under different sky conditions.

In clear sky regions, with ABI's ability to unambiguously characterize these scenes as cloud-free, retrievals are improved merely by forcing the scene to be cloud-free. While statistics in Figs. 10 and 11 indicate that column average biases grow slightly when the ABI cloud mask is used to identify the scene as cloud-free, the profiles themselves show clear improvement above the boundary layer. Near the surface, retrievals are sensitive to the large biases in the prior data in these comparisons, and it is difficult to draw conclusions. Nonetheless, adding three ABI channels slightly decreased overall biases from 0.510 to 0.501 g/kg with about the same error standard deviation of 1 g/kg.

Under cloudy conditions, water vapor retrievals are significantly improved when adding ABI, as shown in Figs. 12 and 13, and results are generally improved when cloud fraction information is added to the retrieval, except for very small cloud fractions where saturation in the cloudy portion of the footprint becomes an issue. Adding cloud top and cloud phase information causes errors larger than 0.5 g/kg. This is likely due to incorrect assumptions about the ice cloud scattering properties.

This study explored the advantages of merging TEMPEST-D, with ABI observations from GOES-16 to improve water vapor soundings. However, ABI-like sensors, whether on the Himawari series satellites (Bessho et al., 2016) or other platforms, cover the entire globe, providing multi-spectral, high spatial, and high temporal observations. While we can only speculate, we assume that hyperspectral IR (Li et al., 2022) planned for the next generation of geostationary satellites will significantly improve the sounding capabilities in clear sky regions. This should lead to better overall retrievals in cloudy skies as well, if one can extrapolate results from Figs. 6 and 7, which show the improvements to the passive MW retrievals when more information is added to the retrievals. With more and more CubeSats being launched, including COWVR and TEMPEST on Space Test Program-Houston 8 (https://podaac.jpl.nasa.gov/COWVR-TEMPEST), TROPICS (Blackwell et al., 2018; https://tropics.ll.mit.edu/CMS/tropics), and the INvestigation of Convective UpdraftS (INCUS; van den Heever et al., 2022; https://incus.colostate.edu) missions, these missions will all benefit from more sounding and cloud information from ABI-like sensors or even from geostationary hyperspectral IR sensors, enhancing the capability of CubeSats.

Code availability

CRTM is available through the website https://github.com/JCSDA/crtm, and MonoRTM can be assessed by the website https://github.com/AER-RC/monoRTM.

Data availability

The TEMPEST-D datasets can be downloaded through the website https://tempest.colostate.edu after registration. The GOES-16 products are archived at CLASS (https://www.avl.class.noaa.gov). The IGRA

668 dataset is available at https://www.ncei.noaa.gov/products/weather-balloon/integrated-global-
669 radiosonde-archive. The ERA5 dataset can be accessed by the website
670 https://www.ecmwf.int/en/forecasts/dataset/ecmwf-reanalysis-v5.
671
672 **Author contribution**
673
674 CPK and CK designed and improved the experiments. CPK is responsible for collecting and processing
675 data. CPK prepared the manuscript. CPK and CK discussed the results and revised the manuscript.
676
677 **Competing interests**
678
679 The contact author has declared that none of the authors has any competing interests.
680
681 **Acknowledgments**
682

683 This study was supported by NASA grant 80NM0078F0617 as part of an effort to improve water vapor
684 soundings from the TEMPEST CubeSat radiometer on Space Test Program-Houston 8. The authors
685 appreciate the reviewers' thorough comments, which greatly improved the paper.

686

687 **References**
688
689 Aires, F.: Measure and exploitation of multisensor and multiwavelength synergy for remote sensing: 1.
690 Theoretical considerations, J. Geophys. Res., 116, D02301–D02301,
691 https://doi.org/10.1029/2010JD014701, 2011.
692
693 Aires, F., Paul, M., Prigent, C., Rommen, B., and Bouvet, M.: Measure and exploitation of multisensor
694 and multiwavelength synergy for remote sensing: 2. Application to the retrieval of atmospheric
695 temperature and water vapor from MetOp, J. Geophys. Res., 116, D02302–D02302,
696 https://doi.org/10.1029/2010JD014702, 2011.
697
698 Aires, F., Aznay, O., Prigent, C., Paul, M., and Bernardo, F.: Synergistic multi-wavelength remote sensing
699 versus a posteriori combination of retrieved products: Application for the retrieval of atmospheric
700 profiles using MetOp-A, J. Geophys. Res., 117, D18304, https://doi.org/10.1029/2011JD017188, 2012.
701
702 Berg, W., Brown, S. T., Lim, B. H., Reising, S. C., Goncharenko, Y., Kummerow, C. D., Gaier, T. C., and
703 Padmanabhan, S.: Calibration and validation of the TEMPEST-D CubeSat radiometer, IEEE Trans.
704 Geosci. Remote Sens., 59, 4904–4914, https://doi.org/10.1109/TGRS.2020.3018999, 2021.
705
706 Bessho, K., Date, K., Hayashi, M., Ikeda, A., Imai, T., Inoue, H., Kumagai, Y., Miyakawa, T., Murata, H.,
707 Ohno, T., Okuyama, A., Oyama, R., Sasaki, Y., Shimazu, Y., Shimoji, K., Sumida, Y., Suzuki, M., Taniguchi,
708 H., Tsuchiyama, H., Uesawa, D., Yokota, H., and Yoshida, R.: An introduction to Himawari-8/9 - Japan's
709 new-generation geostationary meteorological satellites, J. Meteorolog. Soc. Jpn., 94, 151–183,
710 https://doi.org/10.2151/jmsj.2016-009, 2016.
711
712 Blackwell, W. J., Braun, S., Bennartz, R., Velden, C., DeMaria, M., Atlas, R., Dunion, J., Marks, F., Rogers,
713 R., Annane, B., and Leslie, R. V.: An overview of the TROPICS NASA Earth Venture Mission, Q. J. R.
714 Meteorolog. Soc., 144, 16–26, https://doi.org/10.1002/qj.3290, 2018.
715
716 Bohren, C. F. and Huffman, D. R.: Absorption and Scattering of Light by Small Particles, Wiley, New
717 York, 530 pp., https://doi.org/10.1002/9783527618156, 1998.
718
719 Boukabara, S.-A., Garrett, K., Chen, W., Iturbide-Sanchez, F., Grassotti, C., Kongoli, C., Chen, R., Liu, Q.,
720 Yan, B., Weng, F., Ferraro, R., Kleespies, T. J., and Meng, H.: MiRS: An all-weather 1DVAR satellite data
721 assimilation and retrieval system, IEEE Trans. Geosci. Remote Sens., 49, 3249–3272,
722 https://doi.org/10.1109/TGRS.2011.2158438, 2011.
723
724 Boukabara, S.-A., Garrett, K., Grassotti, C., Iturbide-Sanchez, F., Chen, W., Jiang, Z., Clough, S. A., Zhan,
725 X., Liang, P., Liu, Q., Islam, T., Zubko, V., and Mims, A.: A physical approach for a simultaneous retrieval
726 of sounding, surface, hydrometeor, and cryospheric parameters from SNPP/ATMS, J. Geophys. Res.:
727 Atmos., 118, 12,600-12,619, https://doi.org/10.1002/2013JD020448, 2013.
728

729 Boukabara, S.-A., Garrett, K., and Grassotti, C.: Dynamic inversion of global surface microwave
730 emissivity using a 1DVAR approach, Remote Sens., 10, 679–679, https://doi.org/10.3390/rs10050679,
731 2018.
732
733 Brown, S. T., Tanner, A., Reising, S. C., and Berg, W.: Single-point calibration for microwave sounders:
734 Application to TEMPEST-D, J. Atmos. Oceanic Technol., https://doi.org/10.1175/JTECH-D-22-0063.1,
735 2023.
736
737 Clough, S. A., Shephard, M. W., Mlawer, E. J., Delamere, J. S., Iacono, M. J., Cady-Pereira, K.,
738 Boukabara, S., and Brown, P. D.: Atmospheric radiative transfer modeling: A summary of the AER
739 codes, J. Quant. Spectrosc. Radiat. Transfer, 91, 233–244, https://doi.org/10.1016/j.jqsrt.2004.05.058,
740 2005.
741
742 Draine, B. T. and Flatau, P. J.: Discrete-dipole approximation for scattering calculations, J. Opt. Soc. Am.
743 A, 11, 1491, https://doi.org/10.1364/JOSAA.11.001491, 1994.
744
745 Duncan, D. I. and Kummerow, C. D.: A 1DVAR retrieval applied to GMI: Algorithm description,
746 validation, and sensitivities, J. Geophys. Res.: Atmos., 121, 7415–7429,
747 https://doi.org/10.1002/2016JD024808, 2016.
748
749 Elsaesser, G. S. and Kummerow, C. D.: Toward a fully parametric retrieval of the nonraining parameters
750 over the global oceans, J. Appl. Meteorol. Climatol., 47, 1599–1618,
751 https://doi.org/10.1175/2007JAMC1712.1, 2008.
752
753 Field, P. R., Heymsfield, A. J., and Bansemer, A.: Snow size distribution parameterization for midlatitude
754 and tropical ice clouds, J. Atmos. Sci., 64, 4346–4365, https://doi.org/10.1175/2007JAS2344.1, 2007.
755
756 Gambacorta, A., Barnet, C., Wolf, W., Goldberg, M., King, T., Ziong, X., Nalli, N., Maddy, E., and
757 Divakarla, M.: The NOAA Unique CrIS/ATMS Processing System (NUCAPS): First light retrieval results,
758 in: In Proceedings of the ITWG meeting, ITWG, Toulouse, France, 2012.
759
760 GOES-R Series: Mission Requirements Document (MRD) July 28, 2022, 2022.
761
762 Goodman, S. J., Schmit, T. J., Daniels, J., and Redmon, R. J. (Eds.): The GOES-R Series: A New Generation
763 of Geostationary Environmental Satellites, Elsevier, https://doi.org/10.1016/C2015-0-06249-9, 2019.
764
765 Hersbach, H., Bell, B., Berrisford, P., Hirahara, S., Horányi, A., Muñoz-Sabater, J., Nicolas, J., Peubey, C.,
766 Radu, R., Schepers, D., Simmons, A., Soci, C., Abdalla, S., Abellan, X., Balsamo, G., Bechtold, P., Biavati,
767 G., Bidlot, J., Bonavita, M., Chiara, G., Dahlgren, P., Dee, D., Diamantakis, M., Dragani, R., Flemming, J.,
768 Forbes, R., Fuentes, M., Geer, A., Haimberger, L., Healy, S., Hogan, R. J., Hólm, E., Janisková, M., Keeley,
769 S., Laloyaux, P., Lopez, P., Lupu, C., Radnoti, G., Rosnay, P., Rozum, I., Vamborg, F., Villaume, S., and
770 Thépaut, J.: The ERA5 global reanalysis, Q. J. R. Meteorolog. Soc., 146, 1999–2049,
771 https://doi.org/10.1002/qj.3803, 2020.
772

773 Johnson, B. T., Dang, C., Stegmann, P., Liu, Q., Moradi, I., and Auligne, T.: The Community Radiative
774 Transfer Model (CRTM): Community-focused collaborative model development accelerating research
775 to operations, Bull. Am. Meteorol. Soc., https://doi.org/10.1175/BAMS-D-22-0015.1, 2023.
776
777 Kazumori, M. and English, S. J.: Use of the ocean surface wind direction signal in microwave radiance
778 assimilation, Q. J. R. Meteorolog. Soc., 141, 1354–1375, https://doi.org/10.1002/qj.2445, 2015.
779
780 Kulie, M. S., Bennartz, R., Greenwald, T. J., Chen, Y., and Weng, F.: Uncertainties in microwave
781 properties of frozen precipitation: Implications for remote sensing and data assimilation, J. Atmos. Sci.,
782 67, 3471–3487, https://doi.org/10.1175/2010JAS3520.1, 2010.
783
784 Li, J., Schmit, T. J., Jin, X., Martin, G., and Li, Z.: GOES-R Advanced Baseline Imager (ABI) Algorithm
785 Theoretical Basis Document for Legacy Atmospheric Moisture Profile, Legacy Atmospheric
786 Temperature Profile, Total Precipitable Water, and Derived Atmospheric Stability Indices, Version 3.1,
787 2019.
788
789 Li, J., Menzel, W. P., Schmit, T. J., and Schmetz, J.: Applications of geostationary hyperspectral infrared
790 sounder observations: Progress, challenges, and future perspectives, Bull. Am. Meteorol. Soc., 103,
791 E2733–E2755, https://doi.org/10.1175/BAMS-D-21-0328.1, 2022.
792
793 Liu, G.: A database of microwave single-scattering properties for nonspherical ice particles, Bull. Am.
794 Meteorol. Soc., 89, 1563–1570, https://doi.org/10.1175/2008BAMS2486.1, 2008.
795
796 Liu, Q., van Delst, P., Chen, Y., Groff, D., Han, Y., Collard, A., Weng, F., Boukabara, S.-A., and Derber, J.:
797 Community Radiative Transfer Model for radiance assimilation and applications, in: IGARSS 2012 - 2012
798 IEEE International Geoscience and Remote Sensing Symposium, Munich, Germany, 3700–3703,
799 https://doi.org/10.1109/IGARSS.2012.6350612, 2012.
800
801 Ma, Z., Li, Z., Li, J., Schmit, T. J., Cucurull, L., Atlas, R., and Sun, B.: Enhance low level temperature and
802 moisture profiles through combining NUCAPS, ABI observations, and RTMA analysis, Earth Space Sci., 8,
803 https://doi.org/10.1029/2020EA001402, 2021.
804
805 Milstein, A. B. and Blackwell, W. J.: Neural network temperature and moisture retrieval algorithm
806 validation for AIRS/AMSU and CrIS/ATMS, J. Geophys. Res.: Atmos., 121, 1414–1430,
807 https://doi.org/10.1002/2015JD024008, 2016.
808
809 Nowell, H., Liu, G., and Honeyager, R.: Modeling the microwave single-scattering properties of
810 aggregate snowflakes, J. Geophys. Res.: Atmos., 118, 7873–7885, https://doi.org/10.1002/jgrd.50620,
811 2013.
812
813 Padmanabhan, S., Gaier, T. C., Tanner, A. B., Brown, S. T., Lim, B. H., Reising, S. C., Stachnik, R., Bendig,
814 R., and Cofield, R.: TEMPEST-D radiometer: Instrument description and prelaunch calibration, IEEE
815 Trans. Geosci. Remote Sens., 59, 10213–10226, https://doi.org/10.1109/TGRS.2020.3041455, 2021.
816

817 Radhakrishnan, C., Chandrasekar, V., Reising, S. C., and Berg, W.: Rainfall estimation from TEMPEST-D
818 CubeSat observations: A machine-learning approach, IEEE J. Sel. Top. Appl. Earth Obs. Remote Sens.,
819 15, 3626–3636, https://doi.org/10.1109/JSTARS.2022.3170835, 2022.
820
821 Reising, S. C., Gaier, T. C., Padmanabhan, S., Lim, B. H., Heneghan, C., Kummerow, C. D., Berg, W.,
822 Chandrasekar, V., Radhakrishnan, C., Brown, S. T., Carvo, J., and Pallas, M.: An earth venture in-space
823 Technology Demonstration Mission for Temporal Experiment for Storms and Tropical Systems
824 (TEMPEST), in: IGARSS 2018 - 2018 IEEE International Geoscience and Remote Sensing Symposium,
825 Valencia, 6301–6303, https://doi.org/10.1109/IGARSS.2018.8517330, 2018.
826
827 Ringerud, S., Kulie, M. S., Randel, D. L., Skofronick-Jackson, G. M., and Kummerow, C. D.: Effects of ice
828 particle representation on passive microwave precipitation retrieval in a Bayesian scheme, IEEE Trans.
829 Geosci. Remote Sens., 57, 3619–3632, https://doi.org/10.1109/TGRS.2018.2886063, 2019.
830
831 Rodgers, C. D.: Inverse Methods for Atmospheric Sounding: Theory and Practice, World Scientific,
832 Singapore; River Edge, NJ, 238 pp., 2000.
833
834 Schmit, T. J., Li, J., Gurka, J. J., Goldberg, M. D., Schrab, K. J., Li, J., and Feltz, W. F.: The GOES-R
835 Advanced Baseline Imager and the continuation of current sounder products, J. Appl. Meteorol.
836 Climatol., 47, 2696–2711, https://doi.org/10.1175/2008JAMC1858.1, 2008.
837
838 Schulte, R. M. and Kummerow, C. D.: An optimal estimation retrieval algorithm for microwave humidity
839 sounding channels with minimal scan position bias, J. Atmos. Oceanic Technol., 36, 409–425,
840 https://doi.org/10.1175/JTECH-D-18-0133.1, 2019.
841
842 Schulte, R. M., Kummerow, C. D., Berg, W., Reising, S. C., Brown, S. T., Gaier, T. C., Lim, B. H., and
843 Padmanabhan, S.: A passive microwave retrieval algorithm with minimal view-angle bias: Application
844 to the TEMPEST-D CubeSat mission, J. Atmos. Oceanic Technol., 37, 197–210,
845 https://doi.org/10.1175/JTECH-D-19-0163.1, 2020.
846
847 Siddans, R., Gerber, D., and Miles, G.: Optimal Estimation Method retrievals with IASI, AMSU and MHS
848 measurements: Final Report, 2015.
849
850 Siddans, R.: Water Vapour Climate Change Initiative (WV_cci) – Phase One, Deliverable 2.2; Version
851 1.0, 2019.
852
853 Sun, B., Reale, A., Tilley, F. H., Pettey, M. E., Nalli, N. R., and Barnet, C. D.: Assessment of NUCAPS S-NPP
854 CrIS/ATMS sounding products using reference and conventional radiosonde observations, IEEE J. Sel.
855 Top. Appl. Earth Obs. Remote Sens., 10, 2499–2509, https://doi.org/10.1109/JSTARS.2017.2670504,
856 2017.
857
858 Trent, T., Siddans, R., Kerridge, B., Schröder, M., Scott, N. A., and Remedios, J.: Evaluation of
859 tropospheric water vapour and temperature profiles retrieved from MetOp-A by the Infrared and

860   Microwave Sounding scheme, Atmos. Meas. Tech., 16, 1503–1526, https://doi.org/10.5194/amt-16-
861   1503-2023, 2023.
862

863   van de Hulst, H. C.: Light Scattering by Small Particles, Wiley, New York, 470 pp., 1957.
864

865   van den Heever, S., Haddad, Z., Tanelli, S., Stephens, G., Posselt, D., Kim, Y., Brown, S., Braun, S., Grant,
866   L., Kollias, P., Luo, Z. J., Mace, G., Marinescu, P., Padmanabhan, S., Partain, P., Petersent, W., Prasanth,
867   S., Rasmussen, K., Reising, S., Schumacher, C., and the INCUS Mission team: The INCUS Mission, in: EGU
868   General Assembly 2022, EGU22-9021, https://doi.org/doi.org/10.5194/egusphere-egu22-9021, 2022.
869